LRP 708/01 October 2001

Modulated ECH power absorption measurements using a diamagnetic loop in the TCV tokamak

A. Manini, J.-M. Moret, S. Alberti,
T.P. Goodman & M.A. Henderson

Submitted for publication in
Plasma Physics and Controlled Fusion

ISSN 0458-5895

Modulated ECH Power Absorption Measurements using a Diamagnetic Loop in the TCV Tokamak

A Manini, J-M Moret, S Alberti, T P Goodman and M A Henderson

Centre de Recherches en Physique des Plasmas,
Association EURATOM - Confédération Suisse,
École Polytechnique Fédérale de Lausanne,
1015 Lausanne, Switzerland

Abstract. The additional power absorbed by the plasma can be determined from the time derivative of the total plasma energy, which can be estimated from the diamagnetic flux of the plasma using a DiaMagnetic Loop (DML). The main difficulty in using diamagnetic measurements to estimate the kinetic energy is the compensation of the flux measurement sensitivity to poloidal magnetic fields, which is not always easy to adjust. A method based on the temporal variations of the diamagnetic flux of the plasma during Modulated Electron Cyclotron Heating (MECH) has been developed. Using MECH has the advantage that these poloidal fields are not significantly modulated and a good compensation of these fields is not necessary. However, a good compensation of the vessel poloidal image current is crucial to ensure a sufficiently large bandwidth. The application of this diagnostic to studies of the extraordinary mode (X-mode) absorption at the third electron cyclotron harmonic frequency (X3) has been performed on the TCV Tokamak in plasmas pre-heated by X-mode at the second harmonic (X2). A MECH frequency scan has allowed the determination of an optimum modulation frequency, situated at about 200 - 250 Hz. Based on this diagnostic, full single-pass absorption of the injected X3 power was measured with the X2 pre-heating in co-current drive. This high absorption is more than a factor of 2 higher than the one predicted by the linear ray tracing code TORAY. Experimental evidence indicates that a large fraction of the X3 power is absorbed by electrons in an energetic tail created by the X2 pre-heating.

1. Introduction

For the evaluation of the performance of auxiliary heating methods and for the understanding of the transport properties of auxiliary heated plasmas, it is of fundamental importance to determine the fraction of the launched power that is actually transferred to the plasma, as well as where in the plasma the power is deposited. The diagnostic which is probably the best suited for the first goal is the DML providing a measurement of the diamagnetic flux of the plasma, which is directly related to the total plasma kinetic energy.

TCV is equiped with a very versatile Electron Cyclotron Heating (ECH) system. It consists of six gyrotrons operating at the second harmonic, $82.7GHz$, and three gyrotrons at the third harmonic, $118GHz$. The nominal power for each $82.7GHz$ gyrotron is $465kW$ and for each $118GHz$ gyrotron is $480kW$, resulting in a total of radio frequency power of $4.2MW$. In this paper we present the method that has been developed for determining the absorbed power in the ECH experiments in TCV, pointing out especially the results of the first X3 ECH experiments, leaving the problem of the power deposition localisation to other reports [1, 2, 3]. For the determination of the total plasma kinetic energy, the DML has also been used on other devices such as JET [4], ASDEX [5] and TEXTOR [6], but only for this last case modulation experiments have been performed and analysed.

The paper is organised as follows: section 2 presents the MECH experimental scenarios for the X2 and X3 heating configurations; in particular, the X3 absorption is studied varying the X2 pre-heating from purely heating to co (CO-) and counter (CNT-) Electron Cyclotron Current Drive (ECCD). Section 3 explains the analysis of the DML signals. The main problem when using this diagnostic is the compensation of the poloidal fields, which is not an easy task and which limits the absolute precision in the total kinetic energy so derived. In modulation experiments, the variation of this compensation is much smaller than the variation in the diamagnetic flux, thus making a high precision compensation unnecessary. In addition, it is impossible to derive the absorbed power from the increment in the total kinetic energy due to a step change in the absorbed power, since transport mechanisms are known to be dependent on the total input power. MECH is a good solution to these major problems. To bypass the second difficulty the modulation period must be much shorter than the energy confinement time, so that the energy losses during a modulation period can be neglected, thus avoiding the need to precisely know the transport level. Using MECH imposes a consideration of two more details: first of all, a good compensation of the vessel poloidal image current is crucial to ensure a sufficiently large bandwidth allowing the use of high frequency modulations; finally, the modulation period must also be sufficiently long for the deformed electron velocity distribution to relax thus allowing the assumption of an isotropic plasma. Section 4 presents the application of the diagnostic to X3 absorption measurements in X2 pre-heated target plasmas. In particular, single pass absorption and the role of supra-thermal electrons in the absorption are analysed. The power absorption measurements are compared to the power absorption predicted by the ray tracing code TORAY. It is important to underline that for its calculations TORAY assumes a cold plasma as a model for the ray tracing and a warm and fully isotropic plasma for the absorption of the wave. The conclusions are outlined in section 5.

2. Experimental configuration

The method presented in this paper is developed in parallel with the first X3 ECH experiments in TCV [7] and the DML diagnostic is extensively used for power absorption

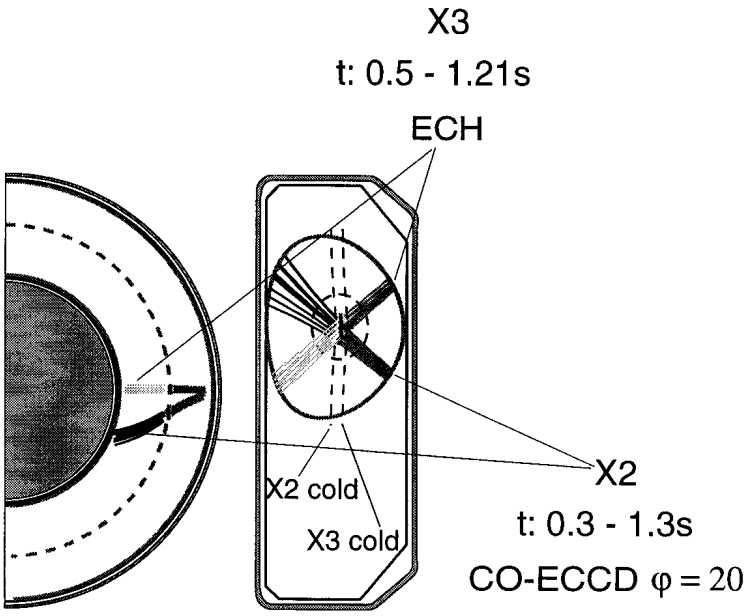

Figure 1. Launching configuration for the X3 absorption measurements in presence of X2 pre-heating. The cold resonances of each harmonic (X2 and X3 cold) are indicated by the vertical dashed lines. The circular dashed line in the poloidal plane indicates the reconstructed $q = 1$ surface. The toroidal angle φ is defined as $\sin\varphi = \frac{\vec{k}\cdot\vec{B}}{|\vec{k}||\vec{B}|}$, where $\vec{k}$ is the k-vector of the X3 wave and $\vec{B}$ is the magnetic field vector.

measurement of X3 ECH in the presence of X2 pre-heating. In these experiments the plasmas are heated using the X3 Electron Cyclotron (EC) X-mode using the first of three X3 gyrotrons [8].

The launching geometry is shown in figure 1. The X3 wave is launched from the low field side via one of the upper lateral launching antennas normally used for X2 heating [9]. A view of the TORAY ray tracing for the X2 and X3 Radio Frequency (RF) beams is shown. The vertical dashed lines passing close to the plasma magnetic axis correspond to the cold resonances of the respective harmonics. The two resonances are spatially separated by approximately $50mm$, and, in the target plasma studied here, they are approximately symmetric with respect to the plasma magnetic axis, the X3 cold resonance being on the low field side. The target plasmas used in the experiments have a major radius $R_0 = 0.88\,m$, a minor radius $a = 0.25\,m$, an elongation $\kappa = 1.31$, a toroidal field $B_0 = 1.42\,T$ and an electron density $n_{e0} = 2.5 \cdot 10^{19}\,m^{-3}$. The evolution of relevant plasma parameters is shown in figure 2. The X3 waves are injected in plasmas pre-heated with second harmonic X-mode. The X2 pre-heating is kept at a constant power level from 0.3 to $1.3\,s$ whereas the X3 power is applied from 0.4 to $1.2\,s$ and includes a $150 - 200\,ms$ phase with 100 % power amplitude modulation.

A modulation frequency scan was performed using frequencies between 20 and

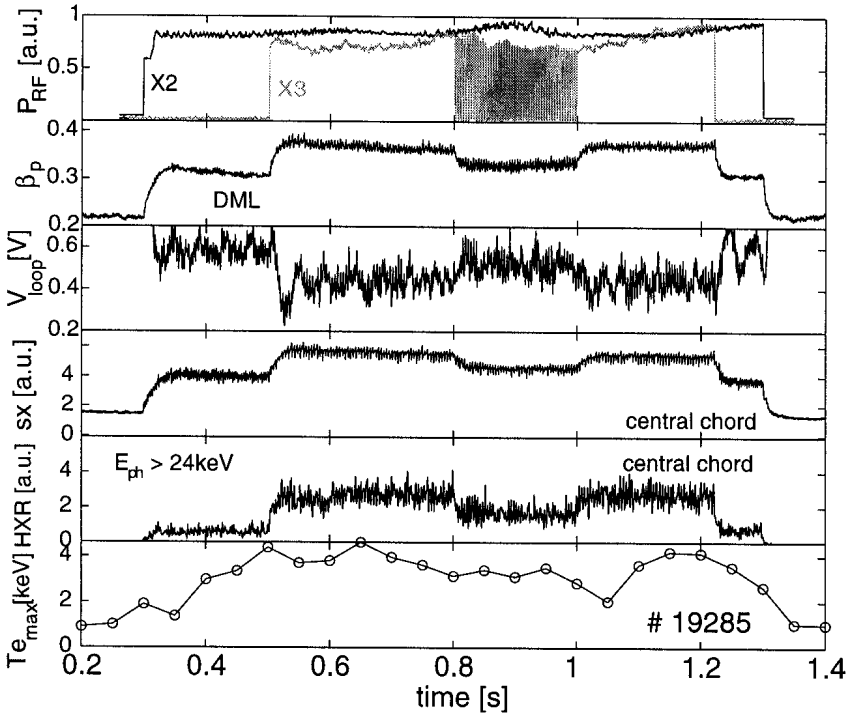

Figure 2. Typical time traces for the X2 and X3 ECH. From top to bottom: X2/X3 RF power, poloidal beta, loop voltage, soft and hard x-ray signals, electron temperature $T_e(0)$ (measurement taken every $50\,ms$). RF power: $P_{X2} \approx P_{X3} = 0.47MW$. Plasma current: $I_p = 200kA$, line average density $\overline{n_e} = 2 \times 10^{19} m^{-3}$.

$700\,Hz$. It is not useful to use higher values because of the limited DML frequency response and the small signal to noise ratio at higher frequencies. The large variations of the central electron temperature $T_e(0)$, measured by Thomson scattering, are produced by the sawteeth. In this experiment the level of sawtooth activity does not strongly perturb the DML signal. However, in case of strong sawtooth activity, the effect on the DML diagnostic is significantly increased.

3. Analysis procedure

3.1. Frequency response of the DML

The diamagnetic loop system, shown in figure 3, consists of two loops, a first one (1-turn) wound around the vacuum vessel, labelled DML, and a second one serving as a compensation loop, labelled CL.

The DML loop measures the plasma diamagnetic flux $\Delta\phi$, but also some toroidal flux from the toroidal field coil current I_t, and from the poloidal image current in the vessel, I_ν. The characteristic decay time constant of the vessel current is around $5.3\,ms$ and if not treated correctly it would limit the bandwidth of the measurement to far below $30\,Hz$.

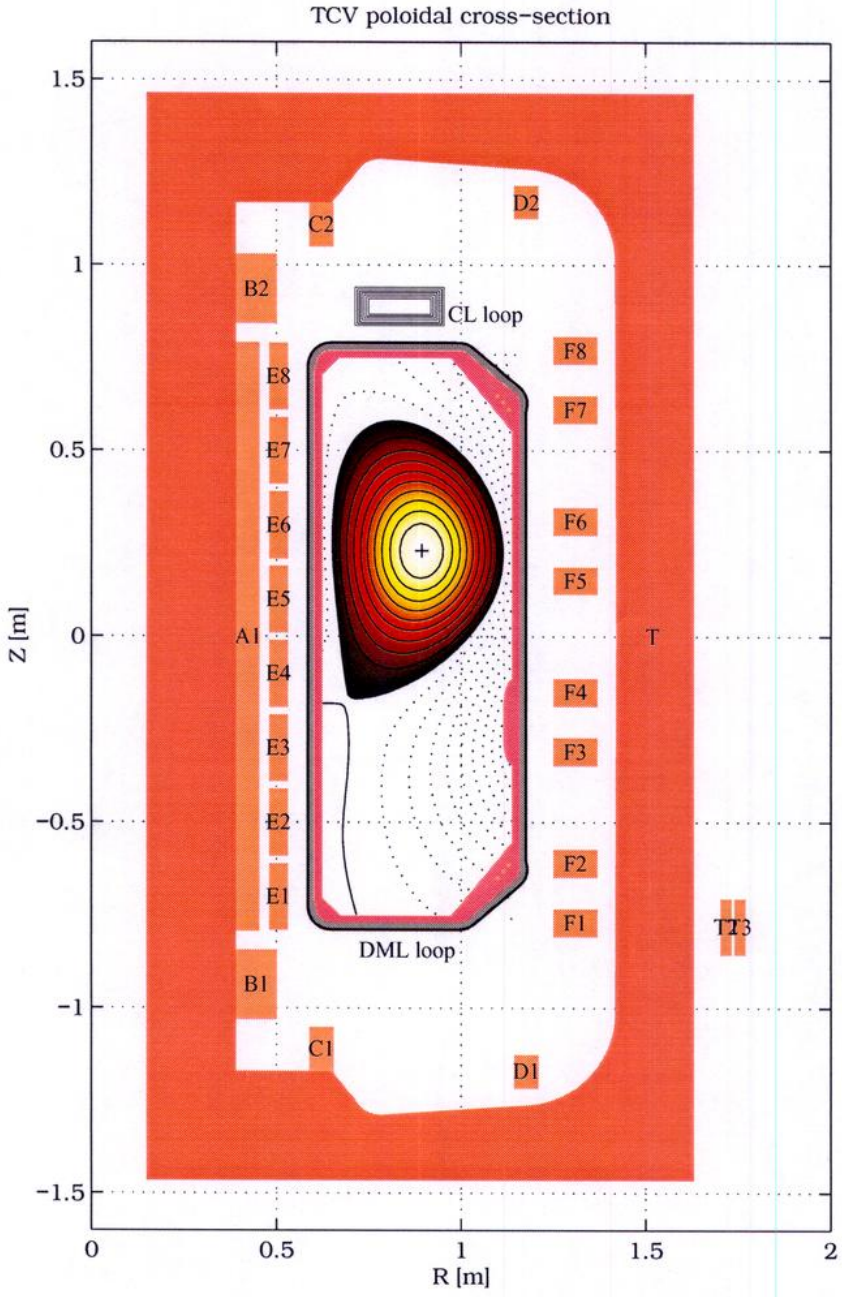

Figure 3. The DML diagnostic configuration on TCV. The loop labelled DML is the 1-turn diamagnetic loop, while the one labelled CL is the compensation loop.

The voltages and currents generated in these two loops and in the vessel obey the following circuit equations:

$$\begin{bmatrix} U_D \\ U_C \\ 0 \end{bmatrix} = \begin{bmatrix} s & sM_{Dt} & sM_{D\nu} \\ 0 & sM_{Ct} & 0 \\ s & sM_{\nu t} & sL_\nu + R_\nu \end{bmatrix} \begin{bmatrix} \Delta\phi \\ I_t \\ I_\nu \end{bmatrix}. \tag{1}$$

The mutual inductances between the various circuits are symbolised by M, the self

inductance and poloidal resistance of the vessel by L_ν and R_ν, and s is the Laplace variable. Solving for the plasma diamagnetic flux yields:

$$\Delta\phi = \frac{1+s\tau_\nu}{1+s\tau_1}\frac{U_D}{s} - \frac{1+s(\tau_\nu-\tau_2)}{1+s\tau_1}\frac{M_{Dt}}{M_{Ct}}\frac{U_C}{s} \tag{2}$$

where $\tau_\nu = L_\nu/R_\nu$, $\tau_1 = (L_\nu - M_{D\nu})/R_\nu$ and $\tau_2 = (M_{D\nu}M_{\nu t})/(M_{Dt}R_\nu)$. For practical reasons of the large amplitude range of the induced signals, partial compensation and integration are performed in analog hardware according to:

$$\Delta\phi_a = \frac{1}{s}(U_D - \frac{M_{Dt}}{M_{Ct}}U_C) + \frac{\tau_2}{1+s(\tau_\nu-\tau_2)}U_D. \tag{3}$$

Based on this signal the plasma flux is derived by digital signal processing implementing the transfer function:

$$\Delta\phi = \frac{1+s(\tau_\nu-\tau_2)}{1+s\tau_1}\Delta\phi_a. \tag{4}$$

Since the DML loop is wound directly on the vessel and follows a path very close to that of the vessel current, $M_{D\nu}$ and L_ν are almost identical and τ_1 is very small. Neglecting $(\tau_\nu - \tau_2)$, which is of the order of $\tau_\nu/30$, in equations (3) and (4) would introduce an error in the estimated plasma flux which can be directly derived from equation (2) as

$$s(\tau_\nu - \tau_2)M_{Dt}I_t. \tag{5}$$

It is important to remember that the flux from the toroidal field coil current $M_{Dt}I_t$ is 10^4 times larger than $\Delta\phi$, which implies that this error is not negligible at all. However it influences the measurements only via a time variation of I_t and not in principle from a time variation of the plasma flux. Nevertheless, since the toroidal field coils are driven by rectifier power supplies, this noise would dominate the signal and make its analysis impossible. Moreover, dynamic measurements require a good compensation of the vessel poloidal image current which arises from both the AC component of the toroidal magnetic field and the variation of the plasma diamagnetic flux. On TCV the second order analog compensation makes the bandwidth of the diagnostic high enough to make the power modulation measurement possible.

3.2. Modulation of diamagnetic flux and plasma energy

The derivation of the relation between the plasma energy and the diamagnetic flux, required to deduce the plasma energy variations induced by the modulated ECH power, can be found in Appendix A. The relationship between the different parameters is (A.11):

$$W = \frac{3}{4}\frac{B_{pa}^2 V_p}{2\mu_0}\left[S_1 + S_2\left(1 - \frac{R_t}{R_0}\right)\right] + \frac{3\pi}{\mu_0}B_{t0}R_0 \cdot \Delta\phi \tag{6}$$

where W is the total plasma kinetic energy, V_p the plasma volume, S_1 and S_2 the well known Shafranov surface integrals (A.4) and (A.5), R_t a characteristic radius

defined in (A.6), R_0 and B_{pa} the constant major radius and the poloidal magnetic field for normalisation, B_{t0} the vacuum toroidal magnetic field at R_0 and $\Delta\phi$ the diamagnetic flux. Taking the Fourier transformation of equation (6) and assuming that the modulation of $S^* = S_1 + [S_2(1 - R_t/R_0)]$ is negligible, we obtain

$$\tilde{W} = \frac{3\pi}{\mu_0} B_{t0} R_0 \cdot \Delta\tilde{\phi}. \tag{7}$$

where the $\tilde{}$ denotes the modulation contribution to the different signals. We can only simplify (6) to (7) if $\tilde{S}^* = 0$ (see Appendix A). Figure 4 shows that the contribution to the signal produced by the modulation of the Shafranov integrals is negligible (less than 10%). The calibration factor in equation (7) is therefore very simple.

As mentioned, the main difficulty in using diamagnetic measurements to estimate the kinetic energy is the compensation of the flux measurement for "parasitic" poloidal magnetic fields. In the case of power modulation, these fields are not significantly modulated and a good compensation of this modulated contribution is not required (see figure 5).

3.3. Modelling of the power balance equation

The analysis procedure can be divided into two different parts. In a first step the power balance equation is analysed, which allows the determination of the experimental requirements for the modulation frequency. In the second step (described in Appendix B), the plasma energy response to the injected ECH power modulation is extracted. Hence, the decomposition of the signals allows the determination of the absorbed power as well as the phase difference between the modulated DML energy and the ECH reference signal.

The power balance equations in the perpendicular and parallel directions are given by

$$\frac{dW_{||}}{dt} = -\frac{W_{||}}{\tau_{inc}} + \frac{1}{\tau_{ed}}(\frac{1}{2}W_{\perp} - W_{||}) \tag{8}$$

$$\frac{dW_{\perp}}{dt} = -\frac{W_{\perp}}{\tau_{inc}} + P - \frac{1}{\tau_{ed}}(\frac{1}{2}W_{\perp} - W_{||}). \tag{9}$$

The term P contains the power source which directly increases the perpendicular energy, which in our case is all the additional ECH power [10], $\tau_{inc} = dW\,/\,dP$ is the incremental energy confinement time as defined in [6], τ_{ed} is the electron deflection time which determines the time in which an anisotropy of the plasma (given by the term $\frac{1}{2}W_{\perp} - W_{||}$) can be mantained in the presence of pitch angle scattering. The total plasma energy is given by $W = W_{||} + W_{\perp}$.

Assuming a fully isotropic plasma, i.e. if $\tau_{ed} \to 0$ and $(\frac{1}{2}W_{\perp} - W_{||}) \to 0$, then equations (8) and (9) can be simplified, after Fourier transformation, to

$$\tilde{W} = \frac{1}{i\omega + 1\,/\,\tau_{inc}} \cdot \tilde{P} \equiv H1 \cdot \tilde{P} \tag{10}$$

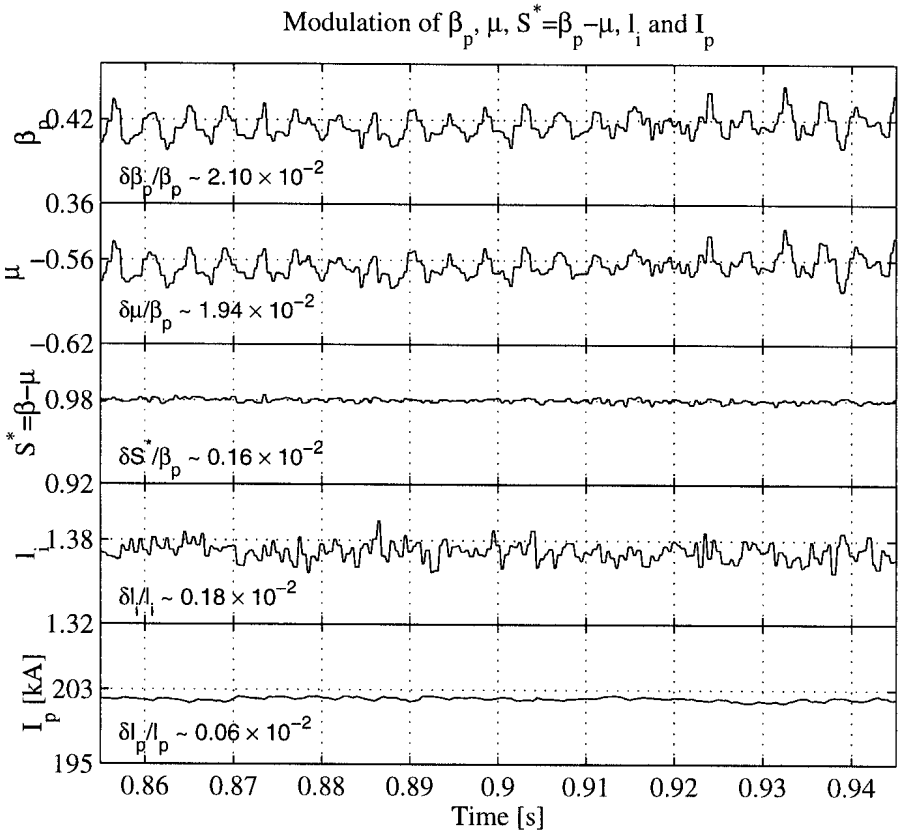

Figure 4. Influence of the modulation on important plasma parameters, such as poloidal beta β_p, plasma diamagnetism μ, Shafranov surface integrals S^*, plasma internal inductance l_i and current I_p. The comparison of the different contributions to the poloidal beta (see equation (A.7)) shows that the main contribution is given by the diamagnetic term.

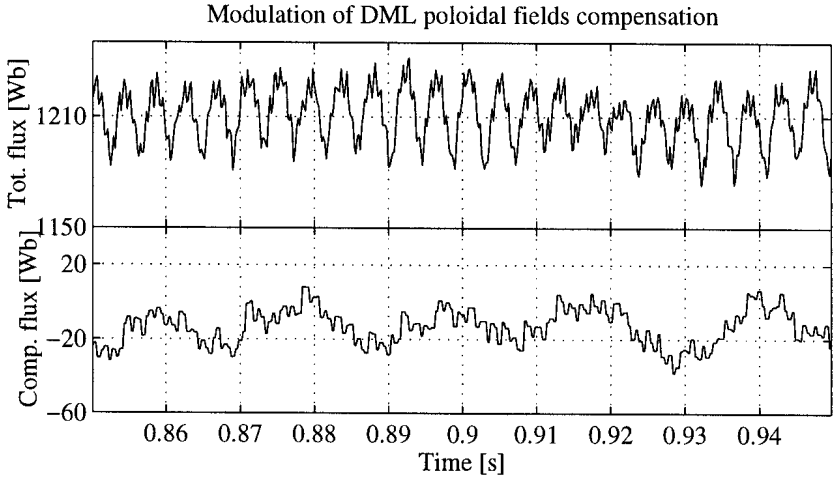

Figure 5. Modulation induced on the total flux and on the compensation flux. Comparing the amplitude induced by the modulation shows that the influence on the compensation flux is negligible.

where $H1$ is the transfer function so defined. Hence, if the modulation frequency is large enough that the energy losses in one cycle can be ignored, i.e. if

$$\omega\tau_{inc} \gg 1 \tag{11}$$

then we obtain

$$\tilde{W} = -\frac{i}{\omega}\tilde{P}. \tag{12}$$

This simple relationship is valid for any frequency satisfying (11) but only for a fully isotropic plasma. Now, having the possibility of deriving $\tilde{W}$ from the DML, we can then determine the injected power. The calculation reduces to multiplying the modulation contribution to the plasma energy by the modulation frequency, $|\tilde{P}| = \omega \cdot |\tilde{W}|$, with the phase difference between the energy modulation contribution and the injected power modulation contribution being 90^o.

Let us now analyse the more realistic case in which both the incremental energy confinement time τ_{inc} and the pitch angle scattering time τ_{ed} have to be considered. Taking the Fourier transformation of equations (8) and (9) and combining them, we obtain

$$\tilde{W}_\perp = \frac{2\tau_{inc}(i\omega\tau_{inc}\tau_{ed} + \tau_{ed} + \tau_{inc})}{-2\omega^2\tau_{inc}^2\tau_{ed} + 4i\omega\tau_{inc}\tau_{ed} + 3i\omega\tau_{inc}^2 + 2\tau_{ed} + 3\tau_{inc}}\tilde{P} \equiv H2 \cdot \tilde{P} \tag{13}$$

where ω is the modulation frequency and $H2$ the transfer function. To determine the degree of anisotropy of the plasma, the transfer function $H2$ is analysed with the help of figure 6, where

$$H3 = \frac{1}{i\omega + 1\,/\,\tau_{inc}^*} \tag{14}$$

with $1\,/\,\tau_{inc}^* = 1\,/\,\tau_{inc} + 1\,/\,\tau_{ed}$. The curves in figure 6 are calculated with $\tau_{inc} = 2\,ms$, which is approximately the incremental energy confinement time of the ECH discharges in TCV, and $\tau_{ed} = 230\,\mu s$, which is an upper limit estimation of the pitch angle scattering time for these discharges (see Appendix C). For other TCV discharges where the density is lower (i.e. $n_e = 1.5 \cdot 10^{19}\,m^{-3}$),the electron temperature is higher (i.e. $T_e = 12\,keV$) and the supra-thermal electrons have higher energy $T_e^* = 50\,keV$, the pitch angle scattering time becomes $\tau_{ed} \approx 900\,\mu s$, which is much closer to the modulation frequencies used. Hence, the determination of an adequate modulation frequency becomes less obvious and a more careful frequency scan would have to be performed.

The limit expressed by equation (12) is plotted in the figure as transfer function $H1$. For $\omega \to 0$ the amplitude of $H1$ deviates from the $1\,/\,\omega$ dependence because the modulation frequency is not high enough to avoid energy losses; meanwhile the phase decreases towards zero. For $\omega \to \infty$, amplitude and phase show an asymptotic behaviour towards $1\,/\,\omega$ and 90^o respectively. The dashed line $H2$ expresses on the other hand the more realistic transfer function (13). For $\omega \to 0$ the phase shows the same ω-dependence as for $H1$, while the amplitude tends to reach a value which is lower than the previous one since only the perpendicular energy is contained. The relation

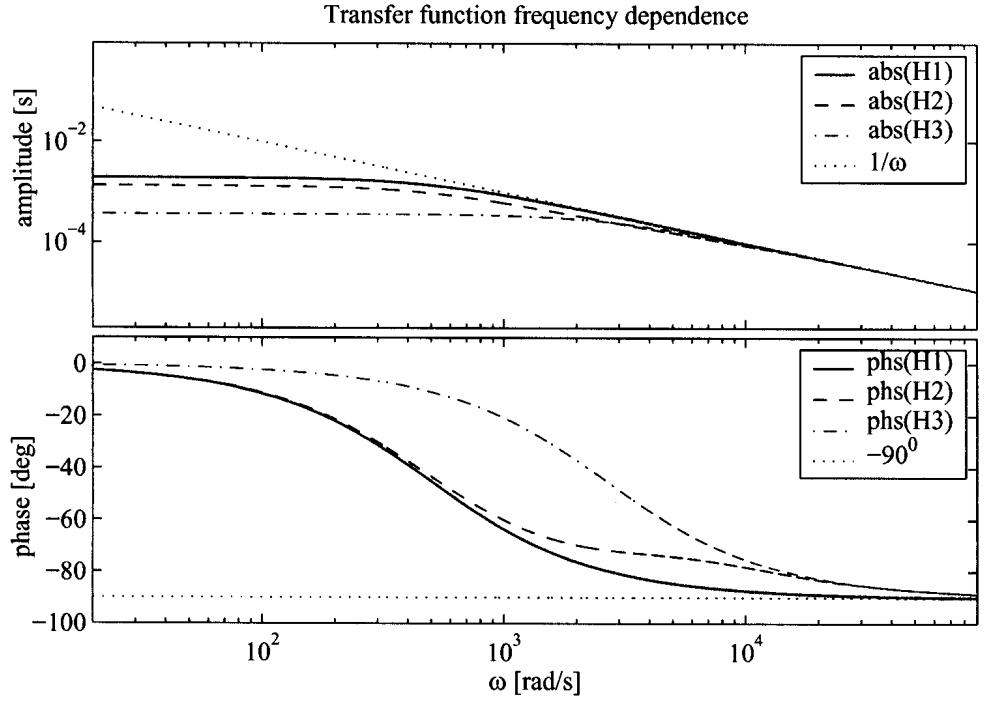

Figure 6. Frequency dependence of the different limits of the transfer function. For $\omega \to 0$ the influence of energy losses decreases the amplitude and forces the phase to 0^o. On the other hand, for $\omega \to \infty$ the amplitude points asymptotically to $1/\omega$ while the phase to 90^o.

between the two limits is $|H1| = 3/2 \cdot |H2|$, which is in agreement with the fact that $H1$ represents the transfer function of the total energy W, while $H2$ represents the transfer function of the perpendicular energy $W_\perp$ only, for which the relation $W = 3/2 \cdot W_\perp$ holds (for an isotropic plasma). The $3/2$ proportionality factor holds up to about $\omega = 3000\, rad/s$, which means that for all the frequencies used the approximation used in (A.11) is justified when the phase is close to 90^o. Finally, the line $H3$ expresses the limit $\tau_{ed} \gg \tau_{inc}$, which in fact implies $\tilde{W}_{||} \to 0$. The behaviour of the $H2$ phase above $1000\, rad/s$ is understood from the behaviour of $H3$: when the modulation period becomes comparable to the pitch angle scattering time, this produces a "slowing down" of the phase decrease towards 90^o. The asymptotic tendency of $H2$ for $\omega \to \infty$ then follows the one for $H3$. Hence, the final requirements for the modulation is

$$\frac{1}{\tau_{ed}} \gg \omega \gg \frac{1}{\tau_{inc}} \tag{15}$$

i.e. the modulation period must be smaller than the mean energy confinement time but much larger than the pitch angle scattering time. The modulation frequency used for the detailed analysis of the X3 absorption is $237\, Hz$ ($\omega = 1500\, rad/s$ whereas $1/\tau_{inc} = 500 s^{-1}$ and $1/\tau_{ed} = 4400 s^{-1}$), which means that for this frequency the use of expression (12) for the calculation of the absorbed power is justified.

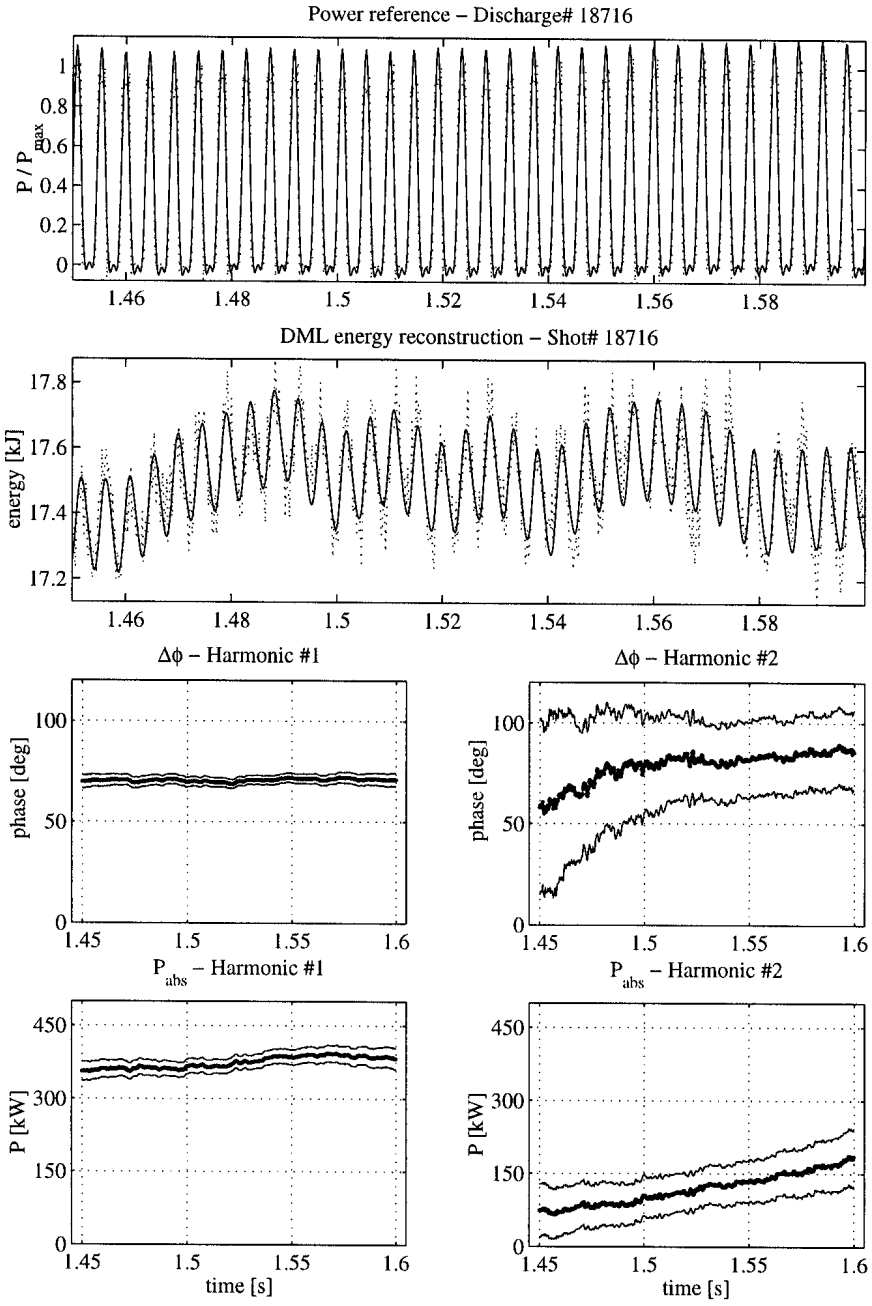

Figure 7. Analysis of discharge 18716. (a) ECH power signal modulated at $220Hz$; (b) DML "raw" and "reconstructed" signal; (c) and (d) phase and amplitude time evolution of the first two MECH harmonics (ω and 2ω). X2 heating configuration: $1.2\,MW$ constant power followed by $0.4\,MW$ modulation.

3.4. Application of the model to a X2 MECH discharge

As an example of the output and to illustrate the validity of the whole procedure, a typical result of the calculations performed for the $220\,Hz$ X2 modulation part of a discharge is shown in figure 7. The top signal (7a) is the ECH power signal which is

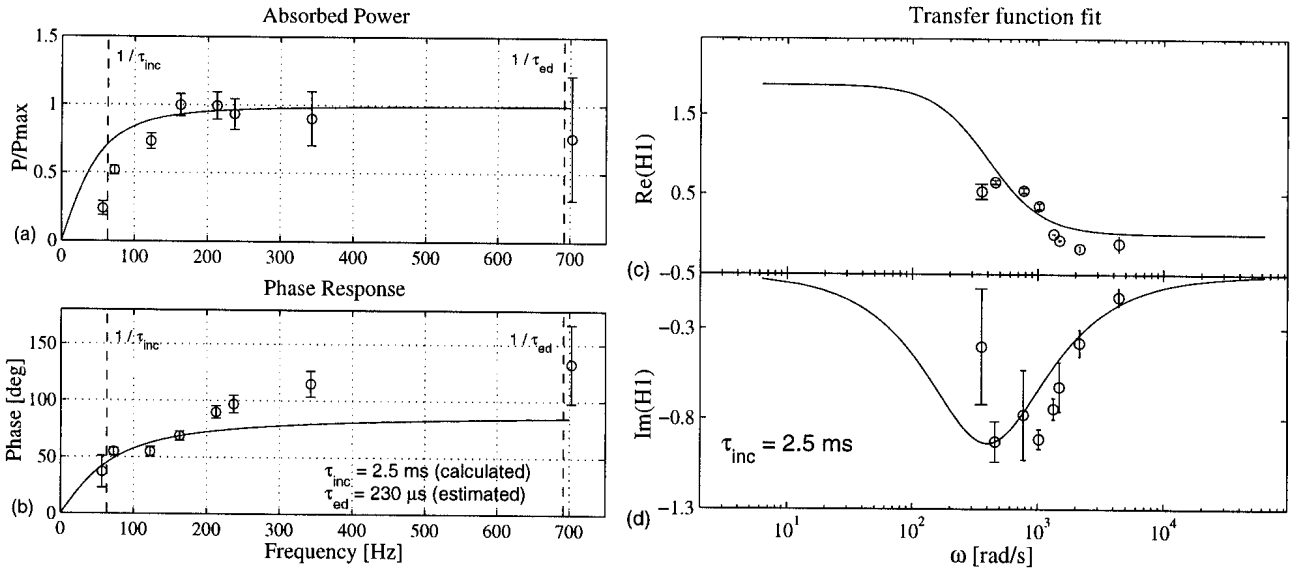

Figure 8. Power absorption frequency scan. (a) Averaged power absorption; (b) phase response. The lines correspond to the fitted amplitude and phase. For the calculation of the incremental electron energy confinement time, the fit of the experimental data has been performed on the real (c) and imaginary (d) parts of the complex experimental transfer function with the model transfer function $H1$.

used as the reference in the analysis of the relative response. The second plot (7b) shows the DML-energy "raw" and "reconstructed" signals. The following (7c) and (7d) show the phase and amplitude time evolution of the relative response of the first two modulation harmonics for the absorbed power. In the last four plots, the thin lines above and below the estimated value display the error bars on the signals, estimated from the standard deviation after the regression. For this particular case, we can restrict our investigation to the fundamental MECH harmonic only.

In this experiment the calculated absorbed power is $375\,kW \pm 15\,kW$, averaged over the whole modulation time interval, with a phase difference of $71^o \pm 4^o$. The phase difference does not reach 90 degrees since in this discharge the X2 power modulation is performed on a $1.2\,MW$ pre-heated plasma which has an incremental energy confinement time of only $\tau_{inc} = 1\,ms$ leading to $\omega\tau_{inc} \cong 1.4 \sim 1$, which means that (11) is not satisfied. Hence, for this particular case, the calculation of the absorbed power is probably under estimated by about 7% (see figure 6), leading to an estimated power absorption of approximately $400\,kW$, so that for X2 experiments, within the experimental error bars, 100% absorption is deduced. For discharges in which the analysis shows larger error bars, these can be reduced by increasing the excitation time interval.

We now turn to one case of X3 modulated power superimposed on a steady X2 pre-heated discharg, in plasmas with $450kW$ of X2 pre-heating in CO-ECCD and $470kW$ of modulated X3 power as shown in figure 1 and 2. Figure 8 shows the results of the

modulation frequency scan performed with frequencies of 19, 73, 123, 163, 213, 237, 343 and $703\,Hz$. The amplitude and phase of the experimental signals determine the complex experimental transfer function. Fitting its real and imaginary parts, shown in (8c) and(8d), allows the determination of the incremental electron energy confinement time. The lines drawn in the figure represent this fit to the experimental data using (10). The incremental electron energy confinement time from this fit is $\tau_{inc} = 2.5\,ms$. The expected behaviour for amplitude (8a) and phase (8b) is observed. For low modulation frequencies the calculated power absorption is lower than the injected power in the range where ω is of the order of $1/\tau_{inc}$. This is confirmed by the phase of the power response, which is below the required 90^o. Above $200\,Hz$, the amplitude and phase saturate. The fitted phase and amplitude are assumed to saturate at 90^o and at the actual power absorbed by the plasma. The saturation of the phase at a value apparently above 90^o is explained by two reasons: first of all, the error bars shown in the figure represent the standard deviation between the energy signal and its fit using (B.1) only; secondly, as the modulation frequency increases, the signal-to-noise ratio for the modulation part decreases significantly. In order to get more precise measurements and smaller error bars, the time window of the MECH and the amplitude of the power modulation should be increased. Analysing the frequency response of higher modulation harmonics allows the determination of the absorbed power at lower frequencies also; for example, the experimental calculation in the $19\,Hz$ discharge used the third MECH harmonic.

4. Application of the DML estimate to X3 absorption measurements

These experiments were aimed at establishing the influence of the plasma conditions on the absorption of X3 ECH power. The plasmas were pre-heated with different power levels of X2 ECH and ECCD. In particular, the X3 power ($0.47MW$) and its toroidal launching angle were kept constant, while different X2 conditions were investigated including variations of the toroidal launching angle, of the power deposition radius and of the total X2 power. For studies of single pass absorption the poloidal angle of the X3 beam was swept in the poloidal plane. For all these cases, the absorbed power is estimated during the modulated portion of the X3 pulse.

4.1. X3 Absorption versus X2 pre-heat power

Figure 9 shows the X3 absorbed power fraction versus the X2 pre-heat power for three X2 launching angles corresponding to central CO-ECCD, ECH and CNT-ECCD. For the three different X2 launching conditions a fit of the global energy confinement time to the injected power of the form $\tau_E = AP_{in}^{\alpha_p}$, yields $A = 4.4 \times 10^{-3}, \alpha_p = -0.75 \pm 0.1$. This is consistent with a previous global energy confinement time scaling [11]. For all these discharges, the measured phase difference between the modulated injected power and the energy modulation was $90^o \pm 10^o$, consistent, within the experimental error bars, with (12) under the condition given by (11). For CO-ECCD target plasmas full

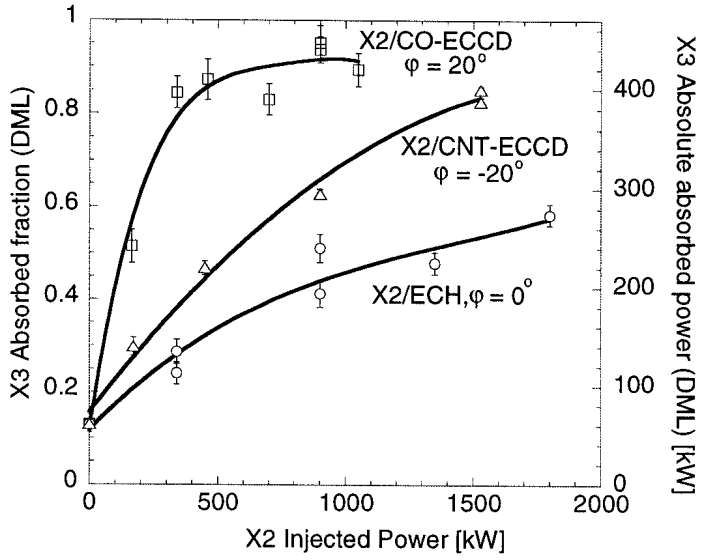

Figure 9. Measured X3 absorption using the DML versus the X2 pre-heat power for three different X2 launching configurations: CO-ECCD ($\varphi = 20^o$), CNT-ECCD ($\varphi = -20^o$) and ECH ($\varphi = 0^o$). The X3 injected power was kept constant at 0.47MW with central deposition and zero toroidal injection angle (ECH). The target plasma is shown in figure 1.

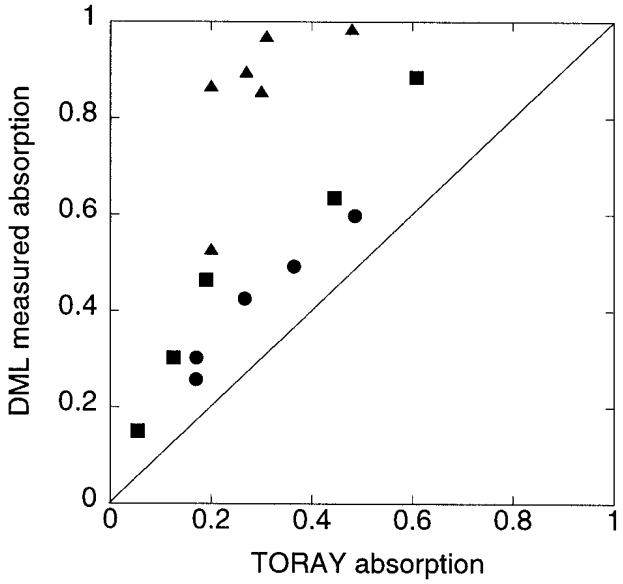

Figure 10. Measured X3 absorption versus calculated absorption with the TORAY code for the shots shown in figure 9. The three different symbols correspond to the following X2 pre-heatings: triangles → CO-ECCD, squares → CNT-ECCD and circles → ECH.

single-pass absorption was obtained.

The absorption calculated with the TORAY code [12], is compared with the measured one in figure 10. The absorption is systematically higher than the TORAY predictions, with the largest discrepancy occurring for the CO-ECCD case which shows

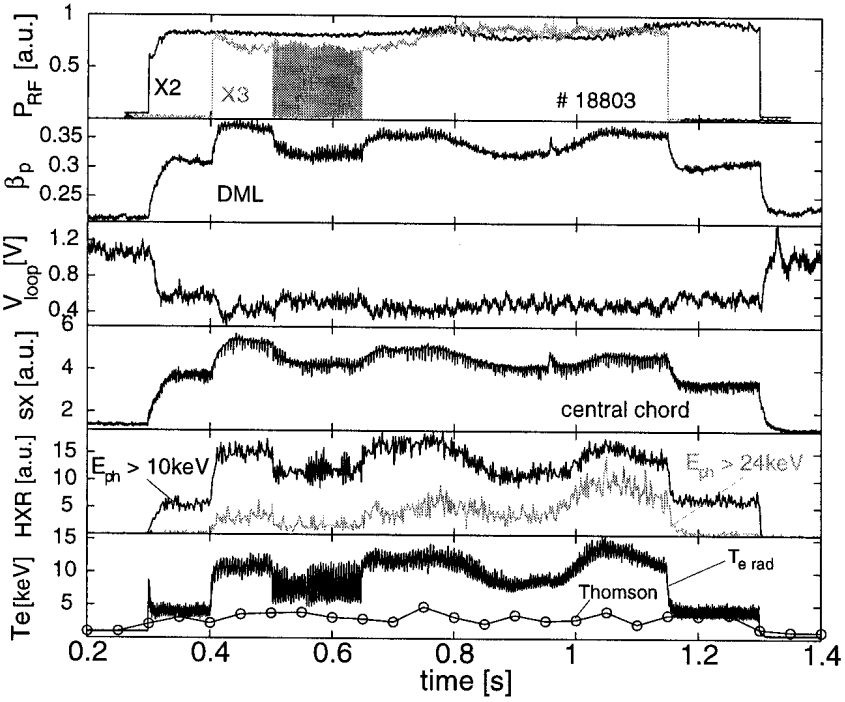

Figure 11. From top to bottom: RF power for X2 and X3, poloidal beta, loop voltage, soft X-ray, two hard X-ray signals for two different photon energy ranges ($E_{ph} > 10keV$ and $E_{ph} > 24keV$), electron temperature T_{e0} (every 50ms), radiation temperature ($T_{e\,rad}$ on a central channel) measured by a high-field side radiometer. The amplitude of the hard X-ray signal for $E_{ph} > 24keV$ is multiplied by 5. RF power: $P_{X2} \approx P_{X3} = 0.47MW$. Plasma current: $I_p = 200kA$, line average density $\overline{n_e} = 2 \times 10^{19} m^{-3}$.

a difference of up to a factor of 3.

4.2. X3 single-pass absorption

An exploration for the estimation of the effect of any second-pass absorption is made by a poloidal scan of the launching angle (from central to off-axis, $r/a > 0.5$) while keeping the X2 beam fixed; the X2 toroidal injection angle is set at $\varphi = 20°$ in CO-ECCD. This is complemented by a polarisation scan of the X3 beam. Typical plasma traces during the poloidal launching angle scan of the X3 beam are shown in figure 11. The poloidal beta is estimated using the DML. The hard X-ray signals are measured with an energy resolving camera [13] and the traces shown correspond to a central chord with different energy filters. The high-field side radiometer (HFS-ECE) [17] views the plasma magnetic axis. Both the hard X-ray diagnostic and the HFS-ECE are sensitive to supra-thermal electrons, whereas the poloidal beta is related to the global plasma energy variation. The radiometer signal is calibrated against $T_e(0)$ during the ohmic phase.

In these discharges the evolution of the X2 and X3 powers is similar to the one shown in figure 2 up to $0.7s$, after which the X3 beam is moved up. The X3 beam

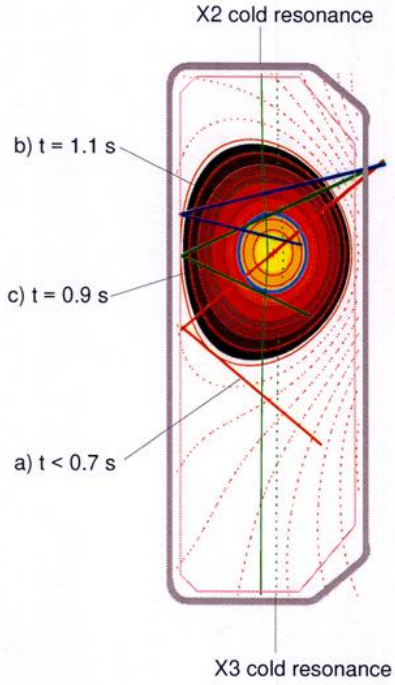

Figure 12. Poloidal scan of the X3 RF-beam with X2 pre-heating at $\phi = 20^o$ (CO-ECCD). Only the central ray trajectory of the X3 beam is shown for three times: (a) $t < 0.7s$, (b) $t = 0.9s$ and (c) $t = 1.1s$.

trajectory at three different times ((a) $t < 0.7s$, (b) $t = 0.9s$ and (c) $t = 1.1s$) is shown in figure 12. As the X3 beam is moved off axis, a clear decrease followed by an increase of the beta poloidal, hard X-ray and HFS-ECE signals is observed from $0.8s$ to $1.1s$. This signal structure can be explained by the fact that, for a Maxwellian distribution function, the X3 optical depth is proportional to the small term $(k_B T_e/m_e c^2)^2$ [14] and as the beam moves away from the region of highest temperature, the optical depth is strongly decreased with an associated weaker absorption. At $t = 1.1s$, the launching angle is such that the beam is reflected by the graphite tiles of the central column and the reflected beam reaches the region of highest temperature on the plasma axis, where efficient absorption again occurs, but from the high field side and with a somewhat less focused beam. For all other times, the beam suffers multiple reflections inside the vacuum vessel and the RF power is eventually absorbed on the vessel walls or partially lost through the different apertures with only a negligible amount absorbed on the X3 resonance layer.

A more quantitative study of the multi-pass absorption has been attempted by varying the X-mode fraction of the injected X3 beam. The X-mode fraction is controlled by a grating polariser in a matching optics unit located at the gyrotron output. Since, for a Maxwellian distribution function, the optical depth of the O-mode fraction is proportional to $(k_B T_e/m_e c^2)^3$ [14], the absorption of this mode is practically zero. The soft X-ray emission viewed on a central chord divided by the line average density follows a similar behaviour as the stored energy variation in the plasma [15]. To use the ΔI_{sxn}

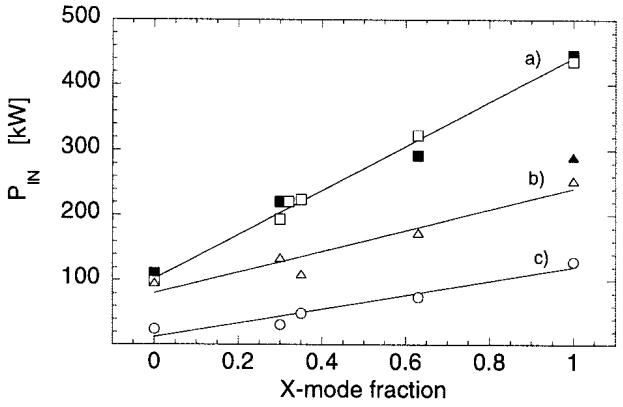

Figure 13. X3 absorption versus X-mode fraction. The filled symbols indicate absorption measurements with the DML, whereas the open symbols are absorption measurements inferred from the variation of the soft X-ray signal, ΔI_{sxn}. The three curves correspond to: (a) central injection ($t < 0.7s$), (b) second pass high-field side absorption ($t \simeq 1.1s$), and (c) off-axis injection ($t \simeq 0.9s$). The filled triangle is an absorption measurement with the DML for high-field side absorption. The continuous lines are linear fits of the ΔI_{sxn} signals.

signal, ΔI_{sxn} being the variation of the soft x-ray emissivity at the turning on of the X3 power, as a measurement of the absorbed power, it is calibrated against the DML for one point of figure 13, where both measurements, DML and ΔI_{sxn}, are available. Curve (a) shows the variation of ΔI_{sxn} at X3 turn-on superposed on the DML absorbed power versus X-mode fraction. Curve (b) (second pass high field side absorption), only shows the ΔI_{sxn} variation versus X-mode fraction with one point measured with the DML (at 100% X-mode). Again good agreement between ΔI_{sxn} and the DML measurement is found where both measurements are available. Finally curve (c) shows ΔI_{sxn} versus X-mode fraction for the case of off-axis injection($t \simeq 0.9s$) with a ray trajectory missing the plasma centre on first and second pass. This last curve shows that, as the beam misses the plasma axis, the multi-pass absorption is negligible. For central first-pass deposition or second-pass high field side deposition, the relatively high absorption in pure O-mode might be associated with the presence of a supra-thermal tail in the electron distribution function generated by the X2 pre-heating [7]. For X-mode central deposition, this study demonstrates that only single pass absorption is being measured.

4.3. X3 absorption versus X2 toroidal injection angle

The dependence of the X3 absorption versus the X2 toroidal injection angle is measured at the same power levels for the two RF harmonics ($P_{X2} \simeq P_{X3} \simeq 470kW$). Figure 14 shows that the DML measurement of the X3 absorbed fraction has an asymmetric dependence on the toroidal injection angle of the X2 beam. The measured X3 absorption (circles) is highest in a target plasma in which the X2 toroidal angle is $\varphi = 20^o$, corresponding to CO-ECCD. For the largest toroidal angle in CO-ECCD ($\varphi = 52^o$),

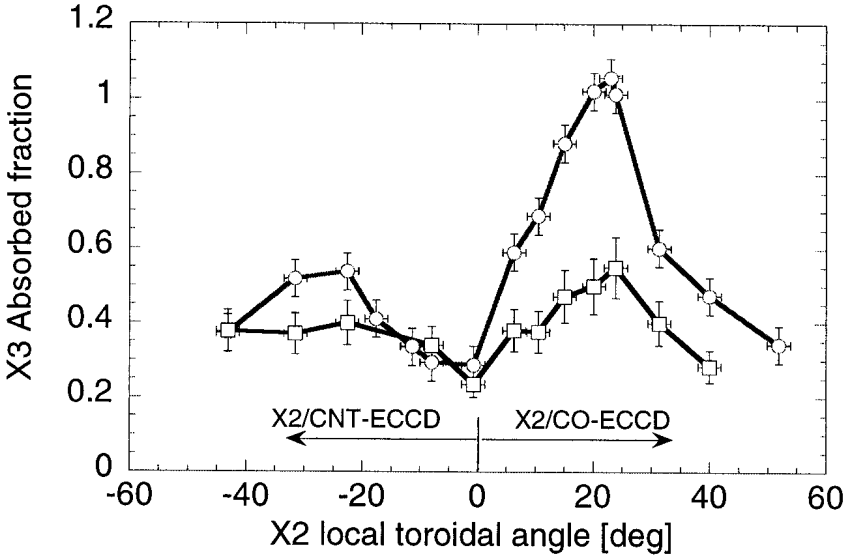

Figure 14. Measured absorption with DML (circles) and calculated absorption with TORAY (squares) versus X2 injection angle. The X2 and X3 injected powers are both at $470kW$. The TORAY code assumes an isotropic Maxwellian distribution function.

significant refraction of the X2 wave occurs with a resulting X2 absorption of only 38% predicted by TORAY. For all other toroidal angles, full single-pass absorption of X2 is predicted.

Calculations of the theoretical absorption with the ray tracing code TORAY are in fair agreement with the experimental results corresponding to ECH ($\varphi = 0^o$) pre-heating. This observation is also in agreement with previous X3 absorption measurements [16]. However, the measured X3 absorption exceeds that predicted by TORAY by a factor of up to 2 for the CNT- and CO-ECCD cases. A likely explanation of the discrepancy is that a large fraction of the X3 power is absorbed by energetic tail electrons created by the X2 ECCD. The presence of these tails is confirmed on both the hard X-ray photon spectra [7, 13] and the high HFS-ECE [7, 17]. A simplified explanation of the possible role of the supra-thermal electrons generated by the X2 pre-heating on the X3 absorption, based on a 1D model, can be found in [8].

5. Conclusion

Modulated ECH has been used to determine the ECH X2 and X3 power absorption from the measurement of the diamagnetic flux variations using the DML. Since only the modulation contribution is relevant to the analysis, the method does not require a perfect compensation of the diamagnetic flux measurement, although a good compensation of the vessel poloidal image current is crucial for ensuring a sufficiently large bandwidth to allow the use of high frequency modulation. The analysis of the behaviour of the amplitude and phase response in the modulation frequency scan has demonstrated the validity of the power absorption calculations with respect to the measured energy

confinement time and the pitch angle scattering time. This scan determined a suitable value for the modulation frequency, situated at about 200 Hz, at which a reasonably high modulation signal-to-noise ratio can still be obtained. The method has been applied to the study of the absorption of the X3 ECH under different X2 pre-heat scenarios. The variations of amplitude and phase as a function of frequency, compared with different models, confirms the validity of the measurements. It has been demonstrated that single-pass absorption of the X3 is measured for central X3 injection with a X2 pre-heating in CO-ECCD, where only 55% absorption is predicted by the ray tracing code TORAY. The discrepancy is explained by the presence of an energetic electron tail generated by the X2 pre-heating. The presence of this tail is confirmed by hard x-ray photon spectrae and by a high filed side ECE radiometer.

Appendix A. Analysis of the diamagnetic flux signal

The diamagnetic flux, which is proportional to the plasma energy, is the difference between the total toroidal flux with plasma and that in the absence of plasma. The plasma energy can be linked to the magnetic field using the force balance between the magnetic force and the kinetic pressure. The integral relations relating the poloidal beta β_p (in particular both the perpendicular and parallel beta $\beta_{p\perp}$ and $\beta_{p||}$), the plasma internal inductance l_i and the plasma diamagnetism μ are derived from the force balance equation in axisymmetric geometry in [18], [19] and [20]. Expressing the equation in cylindrical coordinates (R, Z), we obtain:

$$2\beta_{p\perp} + \beta_{p||} + l_i - \mu = S_1 + S_2 \tag{A.1}$$

$$\beta_{p||} + l_i + \mu = \frac{R_t}{R_0} S_2 \tag{A.2}$$

where

$$[\beta_p, \beta_{p\perp}, \beta_{p||}, l_i, \mu] = \frac{2\mu_0}{B_{pa}^2 V_p} \cdot \int_{\Omega_p} \left[\frac{2p_\perp + p_{||}}{3}, p_\perp, p_{||}, \frac{B_p^2}{2\mu_0}, \frac{B_{tv}^2 - B_t^2}{2\mu_0} \right] dV \tag{A.3}$$

$$S_1 = \frac{1}{B_{pa}^2 V_p} \int_{\delta\Omega_p} B_p^2 (R\hat{e}_R + Z\hat{e}_Z - R_0\hat{e}_R) \cdot \hat{n}\, dS \tag{A.4}$$

$$S_2 = \frac{1}{B_{pa}^2 V_p} \int_{\delta\Omega_p} B_p^2 R_0 \hat{e}_R \cdot \hat{n}\, dS \tag{A.5}$$

$$R_t = \int_{\Omega_p} g\, dV \;/\; \int_{\Omega_p} \frac{g}{R}\, dV \tag{A.6}$$

with R_0 and B_{pa} a constant major radius and a characteristic poloidal magnetic field which cancels out during normalisation, $g = p_{||} + (B_p^2 + B_{tv}^2 - B_t^2) \,/\, 2\mu_0$, B_p, B_t and B_{tv} the poloidal, toroidal and vacuum toroidal magnetic fields respectively, $p_\perp$ and $p_{||}$ the perpendicular and parallel pressure and $\delta\Omega_p$ the surface bounding the plasma volume

Ω_p. Combining (A.1) and (A.2) we obtain the relation between $\beta_{p\perp}$ and the plasma diamagnetism μ

$$\beta_{p\perp} = \frac{1}{2}S_1 + \frac{1}{2}S_2(1 - \frac{R_t}{R_0}) + \mu. \tag{A.7}$$

Under the assumption that $B_{tv} - B_t \ll B_{tv}$, the diamagnetism μ may be approximately related to the diamagnetic flux $\Delta\phi$ through

$$\mu \cong \frac{4\pi B_{t0} R_0 \Delta\phi}{B_{pa}^2 V_p} \tag{A.8}$$

where B_{t0} is the vacuum toroidal magnetic field at R_0 and

$$\Delta\phi = -\int_\Gamma (B_t - B_{tv}) dS. \tag{A.9}$$

Here Γ is the cross-sectional area of Ω_p. The kinetic energy is related to the plasma pressure by

$$W = \frac{3}{2}\int_{\Omega_p} \frac{2p_\perp + p_\parallel}{3}\, dV \tag{A.10}$$

In the case of an isotropic plasma we obtain the final relation between diamagnetic flux and plasma energy, which is

$$W = \frac{3}{4}\frac{B_{pa}^2 V_p}{2\mu_0}\left[S_1 + S_2\left(1 - \frac{R_t}{R_0}\right)\right] + \frac{3\pi}{\mu_0} B_{t0} R_0 \cdot \Delta\phi. \tag{A.11}$$

The measurement of the diamagnetic flux combined with the calculation of the Shafranov surface integrals (A.4) and (A.8) allows the determination of the plasma energy.

Appendix B. Analysis of modulation harmonic response

The problem consists of determining the modulation contributions to each of the signals: the diamagnetic flux, measured with the DML, and the reference ECH power, derived from the tension applied to the gyrotrons cathode. The analysis of these two signals will determine the phase difference between power perturbation and energy response. This analysis method has been developed for the dynamic studies of the plasmas of TCA, and consists of a Harmonic Response Identification Method (HRIM) whose guarding principle is to simultaneously eliminate the base signal (produced by the changes in the main plasma parameters) and extract the complex amplitudes of the harmonics of the modulation frequency [21]. This is expressed mathematically as follows:

$$\tilde{W} = \sum_{n=1}^{N} [Re(U_n)\, \cos n\omega t + Im(U_n)\, \sin n\omega t] + \langle W \rangle \tag{B.1}$$

$$\tilde{P}_{RF} = \sum_{n=1}^{N} [Re(V_n)\, \cos n\omega t + Im(V_n)\, \sin n\omega t] + \langle P_{RF} \rangle \tag{B.2}$$

where U_n and V_n are the complex amplitudes of the harmonics for plasma energy and additional ECH power respectively. We can then evaluate the complex relative response of each harmonic

$$R_n = \frac{U_n}{V_n}. \tag{B.3}$$

$\langle W \rangle$ and $\langle P_{RF} \rangle$ are slowly evolving signals taken as a low order cubic spline.

Appendix C. Estimation of the pitch angle scattering time

The value of τ_{ed} is determined using the following expression for the electron deflection collision frequency [22, 23]:

$$\nu_{ed} = \frac{e^4 n_e (Z_{eff} + 1)\, ln\Lambda}{2\pi\epsilon_0^2 m_e^2} \frac{[\Phi(v^*/v_{th}) - G(v^*/v_{th})]}{v^{*3}} \tag{C.1}$$

where n_e is the electron density and v_{th} the electron thermal velocity. The $*$ quantities refer to the high energy electrons, $ln\Lambda$ is the Coulomb logarithm, $\Phi(x)$ and $G(x)$ are defined by

$$\Phi(x) = \frac{2}{\sqrt{\pi}} \int_0^x exp(-t^2) dt \tag{C.2}$$

$$G(x) = \frac{\Phi(x) - x\Phi'(x)}{2x}. \tag{C.3}$$

The characteristic time related to the pitch angle scattering is then

$$\tau_{ed} = \frac{1}{\nu_{ed}}. \tag{C.4}$$

Typical plasma parameters of the TCV EC heated discharges are: $T_e = 5\,keV$, $T_e^* = 30\,keV$, $n_e = 3 \cdot 10^{19}\,m^{-3}$ and the effective charge of the plasma is estimated as $Z_{eff} = 3$, giving as an upper limit for the pitch angle scattering time a value of $\tau_{ed} \approx 230\,\mu s$. In these conditions the plasma can be assumed to be fully isotropic

Acknowledgments

The authors wish to thank the whole TCV team, the main author in particular the ECRH group, without whom this work would not be possible, and Dr. Jonathan Lister for his precious remarks in writing this paper.
This work was partly supported by the Swiss National Science Foundation.

References

[1] D J Gambier *et al* 1990 *Nuclear Fusion* **30** 23
[2] E Barbato and R Giannella 1985 *Physics-Letters-A* **110A** 309
[3] A Manini *et al* CRPP Internal Report LRP 664/00
[4] G Tonetti *et al* 1986 *Review of Scientific Instruments* **75** 2087
[5] J Gernhardt and F Schneider IPP Report no. IPP III/84

[6] D Lebeau *et al* 1995 *Plasma Phys. Control. Fusion* **37** 1141
[7] S Alberti *et al* , 18th IAEA Fusion Energy Conference Sorrento Italy October 4-10 2000
[8] S Alberti *et al* 2001 Fusion Eng. Design **53** 387
[9] T P Goodman *et al* 1996 *Proc. of the 19th Symposium on Fusion Technology, Lisbon*, ed C Varandas and F Serra (North-Holland, Amsterdam, 1997) p 565
[10] V Erckmann and U Gasparino 1994 *Plasma Phys. Control. Fusion* **36** 1869
[11] A Pochelon *et al* 1999 *Nuclear Fusion* **39** 1807
[12] G R Smith *et al* 1995 *Proc. of the 9th Joint Workshop on ECE and ECRH, Borrego Springs, CA* (World Scientific, Singapore) p 651
[13] S Coda *et al* 2001 *Proc. of the 28th EPS Conference on Controlled Fusion and Plasma Physics, (Madeira, Portugal)*
[14] M Bornatici *et al* 1983 *Nuclear Fusion* **23** 1153
[15] M A Henderson *et al* 2001 Fusion Eng. Design **53** 241
[16] A Pachtman *et al* 1987 *Nuclear Fusion* **27** 1283
[17] P Blanchard *et al* 2001 *Proc. of the 28th EPS Conference on Controlled Fusion and Plasma Physics, (Madeira, Portugal)*
[18] V D Shafranov 1971 *Plasma Physics* **13** 757
[19] L L Lao *et al* 1985 *Nuclear Fusion* 1421
[20] A J Wootton and W A Cooper 1982 *Plasma Physics* **24** 1183
[21] J-M Moret *et al* 1993 *Nuclear Fusion* **33** 1185
[22] L Spitzer Jr 1962 *Physics of Fully Ionized Gases* (Interscience, New York)
[23] D V Sivukhin 1966 *Reviews of Plasma Physics, Vol.4* ed M A Leontovich (Consultant Bureau, New York) p 93